Construction of SnNb$_2$O$_6$ nanosheet/g-C$_3$N$_4$ nanosheet two-dimensional heterostructures with improved photocatalytic activity: Synergistic effect and mechanism insight

Zhengyuan Zhang, Deli Jiang*, Di Li, Minqiang He, Min Chen*

School of Chemistry and Chemical Engineering, Jiangsu University, Zhenjiang 212013, China

ABSTRACT

In this study, novel SnNb$_2$O$_6$/g-C$_3$N 2D/2D nanosheet heterostructures with strong interfacial interaction were successfully constructed by a facile two-step wet chemistry method. The SnNb$_2$O$_6$/g-C$_3$N$_4$ 2D/2D heterostructures exhibit distinctly enhanced visible light photocatalytic performance toward the degradation of methylene blue (MB) as compared to pristine g-C$_3$N$_4$ and SnNb$_2$O$_6$, which can be attributed to the synergistic effect of 2D/2D heterostructures with strong interfacial interaction and abundant 2D coupling interfaces, facilitating efficient charge separation. The optimum photocatalytic activity of 30% SnNb$_2$O$_6$/g-C$_3$N$_4$ heterostructure for the degradation of MB was about 3.9 and 3.2 times higher than those of g-C$_3$N$_4$ and SnNb$_2$O$_6$. It was demonstrated that the photogenerated holes and superoxide radicals are the two main photoactive species toward photocatalytic degradation of MB over the SNO/CN heterostructures. This work may provide some inspiration for the fabrication of 2D/2D nanosheet heterostructures with efficient photocatalytic performance.

1. Introduction

In the past decades, semiconductor-based heterogeneous photocatalysis has attracted increasing attention for its application in environmental purification and solar energy conversion [1–3]. The core target in photocatalysis is the fabrication of an efficient semiconductor-based photocatalyst, which could maximize the efficiency of capture and conversion of solar energy. Various semiconductors including metal oxides, sulfides, nitroxides, and organic metal complexes have been investigated as photocatalysts [4–7]. Among these, as a two-dimensional (2D) conjugated polymer, graphitic carbon nitride (g-C$_3$N$_4$) has emerged as a promising candidate for degradation of organic pollutants, production of H$_2$ from water splitting and photocatalytic conversion of CO$_2$ thanks to its unique electronic band structure and good chemical stability [8–12]. However, the efficiency of single g-C$_3$N$_4$ is still far from satisfactory mainly due to its narrow absorption band and high recombination rate of photogenerated electron–hole pairs [13,14]. Researchers have therefore made significant efforts to improve the photocatalytic efficiency of g-C$_3$N$_4$ by various methods, such as

coupling it with other materials [15–19], nanostructuring [20,21], doping [22,23], and/or copolymerization [24,25].

Coupling 2D layered (nanosheet) materials with other nanostructured semiconductor to form 0D/2D, 1D/2D, and 2D/2D heterostructures has been proven to be a promising way to obtain highly efficient photocatalysts [26–28]. It was well recognized that, due to the 2D structural feature and large surface area, the charge separation efficiency, lifetime of separated charges and visible light response can be improved simultaneously in the 2D nanosheet-based heterostructures. Notably, compared with 0D/2D and 1D/2D heterostructures, the unique 2D/2D (nanosheets on nanosheets) heterostructures possess rather larger surface area and abundant coupling heterointerfaces, which more easily facilitates migration of photogenerated electron–hole pairs, thus contributing to the high photocatalytic activity [29–34]. However, only limited g-C$_3$N$_4$-based 2D/2D heterostructure examples have been demonstrated so far, just limiting in SnS$_2$/g-C$_3$N$_4$ [35], MoS$_2$/g-C$_3$N$_4$ [36,37], MoS$_2$/graphene/g-C$_3$N$_4$ [38], and Co(OH)$_2$/g-C$_3$N$_4$ [19]. Undoubtedly, the fabrication of g-C$_3$N$_4$-based 2D/2D heterojunction photocatalysts with fine interfacial contact and enhanced photocatalytic activity is still in its infancy and remains a significant challenge.

Recently, metal oxide nanosheet prepared by direct synthesis or exfoliation of a layered oxide materials such as niobates or tantalates have attracted a lot of attention in photocatalysis over the past

* Corresponding authors. Fax: +86 511 88791800.
E-mail addresses: dlj@ujs.edu.cn (D. Jiang), chenmin3226@sina.com (M. Chen).

years due to their wide variety of structural and electronic properties and high stability [39–41]. $SnNb_2O_6$, which exhibits a foordite structure where two corner-sharing NbO_6 sheets linked together at their edges and a distorted SnO_8 sheet owing to the existence of a lone-pair electron are alternating, is a promising visible light photocatalyst [42–46]. In this context, $SnNb_2O_6$ nanosheet is probably an ideal candidate to construct 2D/2D heterojuntions with g-C_3N_4 owing to the following reasons: first, it has the suitable band-edge positions with respect to those of CN, which could form type II SNO/CN heterojunction; second, it shows inherently high stability relative to metal sulfate nanosheet materials [47].

Based on the above considerations, in the present work, we demonstrated the construction of novel $SnNb_2O_6$ (abbreviated as SNO) nanosheet/g-C_3N_4 (abbreviated as CN) nanosheet 2D/2D heterostructures with strong interfacial interaction by a simple two-step wet chemistry method. $SnNb_2O_6$ nanosheet material was chosen herein. It was demonstrated that SNO/CN heterostructures exhibited remarkably enhanced visible light photocatalytic activity towards degradation of methylene blue (MB) compared to pristine CN and SNO nanosheets. The synergistic effect of SNO/CN heterostructures with intimate interfacial contact and unique 2D nanosheet heterojunction contributes to the improved separation

efficiency of charge carriers and thus leads to enhanced photocatalytic activity. In addition, the possible photocatalytic mechanism for the degradation of MB was also discussed in detail. It is anticipated that our work could be helpful for the exploration of novel 2D/2D heterojunction photocatalysts with intimate interfacial contact and enhanced photocatalytic activity.

2. Experimental

2.1. Photocatalyst preparation

2.1.1. Materials

Niobium oxide (Nb_2O_5), potassiumhydroxide (KOH), stannous chloride dehydrate ($SnCl_2 \cdot 2H_2O$), hydrochloric acid (HCl), nitric acid (HNO_3), absolute ethanol and urea were purchased from Sinopharm Chemical Reagent Co., Ltd., China and were used as received without any further purification. Deionized water was used in the experiments.

2.1.2. Preparation of SNO/CN heterostructures

CN nanosheets were prepared according to the previously reported method [13]. Typically, 10 g of urea placed in a crucible
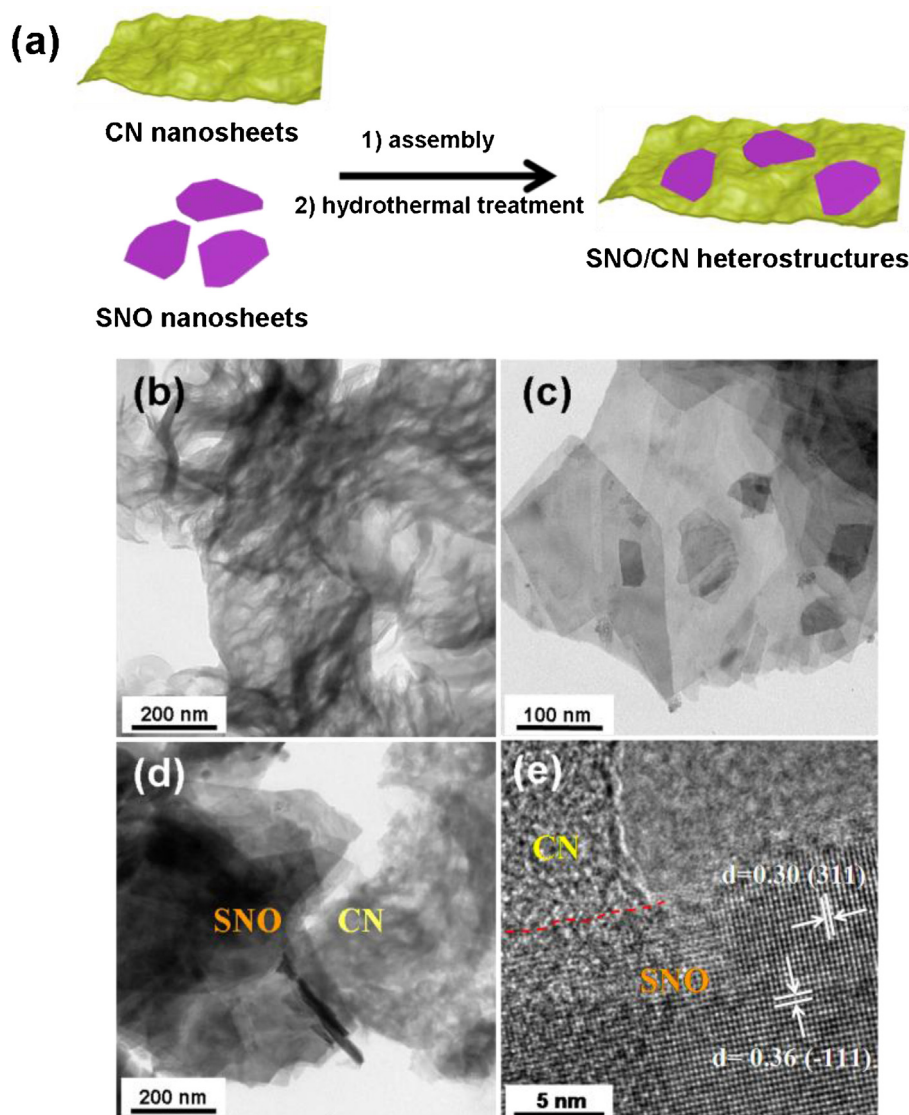

Fig. 1. (a) Schematic illustration of procedure for preparing SNO/CN heterostructures; typical TEM images of (b) CN, (c) SNO, (d) 30% SNO/CN heterostructure, and (e) HRTEM image of 30% SNO/CN heterostructure.
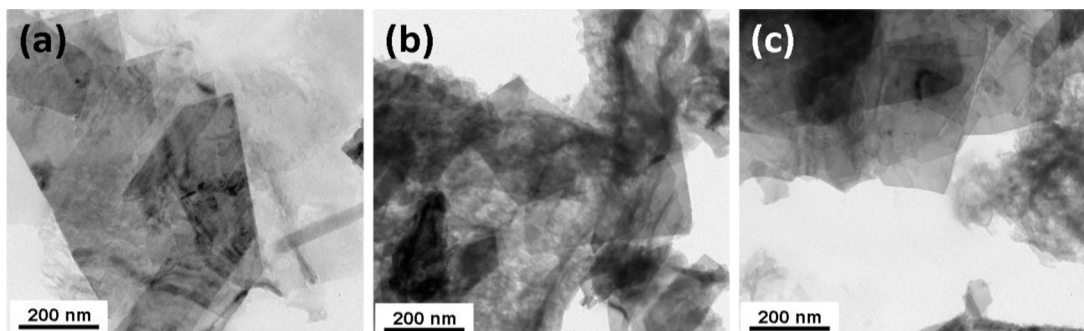
Fig. 2. Typical TEM images of (a) 10% SNO/CN, (b) 20% SNO/CN, and (c) 40% SNO/CN heterostructure.

with a cover was heated to 550 °C at a heating rate of 2.3 °C min^{-1} in a tube furnace for 4 h in air. The resulting final powder was washed with nitric acid (0.1 mol L^{-1}) and distilled water to remove any residual alkaline species adsorbed on the sample surface, and then dried at 80 °C for 24 h.

SNO nanosheets was prepared by a facile hydrothermal reaction using $Nb_2O_5 \cdot nH_2O$ as a precursor which was obtained from a simple procedure reported previously [42]. Typically, 0.5 g of Nb_2O_5 and 2.2443 g of KOH were dispersed in 40 mL distilled water under vigorous stirring for 10 min, then the composites were moved to a 50 mL Teflonlined stainless steel autoclave, followed by heating at 180 °C for 2 days. The pH of the resultant solution was adjusted to 7 using a HCl (2 mol L^{-1}) aqueous solution to obtained $Nb_2O_5 \cdot nH_2O$. After that, 0.4244 g of $SnCl_2 \cdot 2H_2O$ was added into the solution with stirring, the pH values were adjusted to 2 by HCl (2 mol L^{-1}) aqueous solution under vigorous stirring. The above mixed solution was transferred to a 100 mL Teflonlined autoclave immediately and maintained at 200 °C for 48 h in an oven. After cooled naturally,

the products were centrifuged, washed with deionized water and absolute ethanol three times and dried at 60 °C in air.

The SNO/CN heterostructures were fabricated by a facile two-step wet chemistry method (self-assembly followed by hydrothermal treatment). In detail, 0.2 g of the obtained CN was dispersed in 60 mL water with the aid of ultrasonication. At the same time, a certain amount of SNO was dispersed in 20 mL of deionized water by ultrasonication for 30 min. Then, the $SnNb_2O_6$ solution was added into the above g-C$_3$N$_4$ suspension drop by drop and kept stirring for 4 h to get a homogeneous solution. The solution was transferred into a 100 mL Teflonlined stainless steel autoclave and maintained at 160 °C for 12 h. The final mixture was centrifuged at 5000 rpm for 3 min, and fully dried at 60 °C in an oven to get the final SNO/CN heterostructures. To investigate the role of the composition in the photocatalytic performances, the amount of SNO and CN were varied to obtain SNO/CN heterostructures with mass ratios of 10%, 20%, 30%, and 40%, and the samples were labeled as 10% SNO/CN, 20% SNO/CN, 30% SNO/CN, and 40% SNO/CN, respectively.
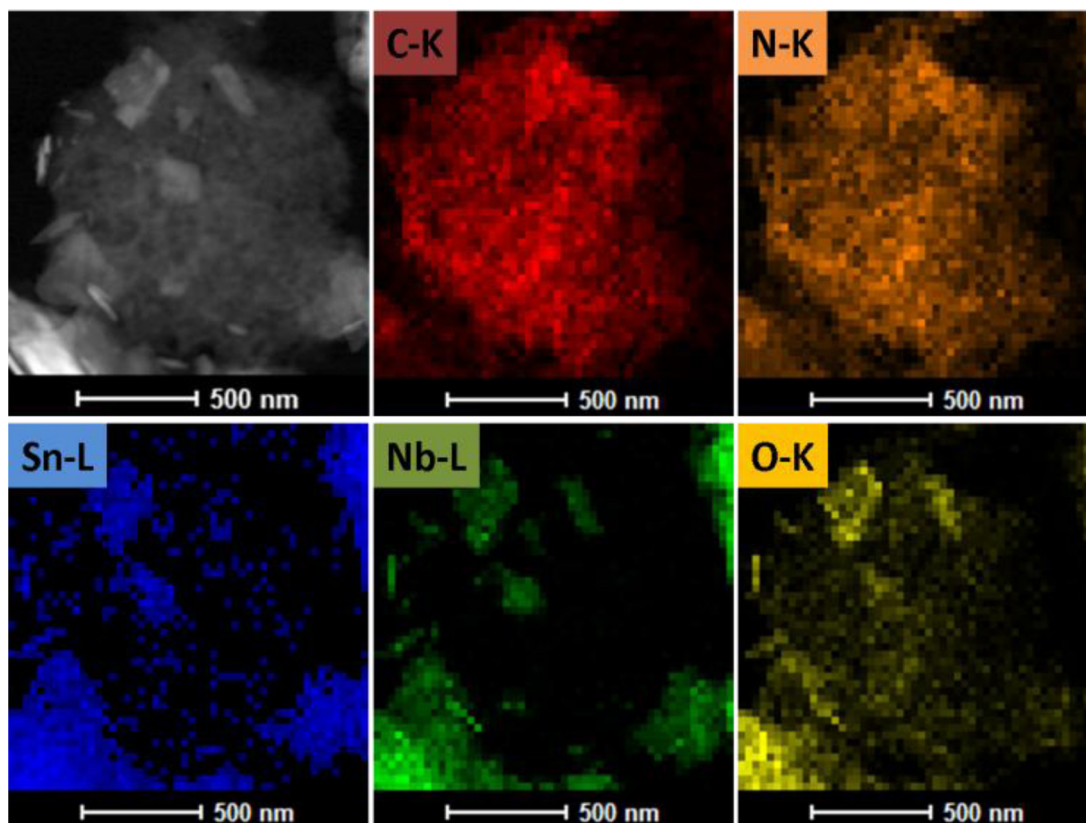

Fig. 3. HAADF-STEM image and the corresponding STEM-EDX elemental mapping images of the 30% SNO/CN heterostructure.

2.2. Characterization

The phase purity and crystal structure of the obtained samples were examined by X-ray diffraction (XRD, Bruker D8 Advance X-ray diffractometer) with Cu-Kα radiation (λ = 1.5406 Å). The morphology of the samples was examined by transmission electron microscopy (TEM; FEI JEM-2100 and FEI Tecnai G2 F20) operated at 200 kV. Surface analysis of the sample was examined by X-ray photoelectron spectroscopy (XPS) using a ESCA PHI500 spectrometer. FT-IR spectrum was performed on a Nicolet FT-IR spectrophotometer (Nexus 470, Thermo Electron Corporation) using KBr disks at room temperature. UV–vis diffuse reflectance spectra (DRS) were performed on a Shimadzu UV-2450 spectrophotometer equipped with spherical diffuse reflectance accessory. The photoluminescence (PL) spectra of the photocatalysts were obtained by a Varian Cary Eclipse spectrometer with an excitation wavelength of 325 nm. The photocurrent and electrochemical impedance spectroscopy (EIS) were measured with an electrochemical analyzer (CHI 660B Chenhua Instrument Company). The electron spin resonance (ESR) signals of radicals spin-trapped by spin-trap reagent DMPO (Sigma Chemical Co.) in water or methanol were examined on a Bruker model ESR JES-FA200 spectrometer.

2.3. Photocatalytic activity

Photocatalytic activity of the sample was evaluated by the degradation MB aqueous solution (10 mg L^{-1}) under irradiation of 500 W tungsten light lamp with a 420 nm cutoff filter. 0.020 g of photocatalyst was suspended into 80 mL of the above MB solution. Prior to irradiation, the suspension was magnetically stirred for 0.5 h in the dark to ensure that the MB could reach the absorption–desorption equilibrium on the photocatalyst surface. Furthermore, all the experiments were performed at 25 °C under constant stirring. During every irradiation interval, about 4 mL of aliquots were sampled and centrifuged to remove the particles. The filtrates were analyzed by a Shimadzu UV-2450 spectrophotometer and the characteristic absorption peak of MB at 664 nm was used to determine the extent of its degradation.

2.4. Photoelectrochemical measurement

To investigate the photoelectrochemical properties of as-prepared samples, the modified electrodes were prepared as follows: 4 mg of the as-prepared photocatalyst was suspended in 1 mL ethanol and 20 μL 5 wt% Nafion solution to produce a slurry. Then, 30 μL of the resulting colloidal dispersion then dropped onto a piece of FTO slice with a fixed area of 1 cm^2. All the photoelectrochemical measurements were measured on an electrochemical analyzer in a standard three-electrode system using the prepared samples as the working electrode, a Pt wire as the counter electrode, and Ag/AgCl as a reference electrode. A 500 W Xe arc lamp served as a light source. The photocurrent and electrochemical impedance spectroscopy (EIS) was performed in 0.2 M Na$_2$SO$_4$ aqueous solution.

3. Results and discussion

3.1. Morphological and structural information

The fabrication procedure of SNO/CN heterostructures is schematically illustrated in Fig. 1a. The morphology and microscopic structure information of SNO, CN, and 30% SNO/CN were characterized by TEM analysis. Fig. 1b shows that the CN sample exhibits wrinkled lamellar structure with relatively smooth surface, which is the typical structural characteristic of CN prepared by the polymerization of urea. As shown in Fig. 1c, the pristine SNO
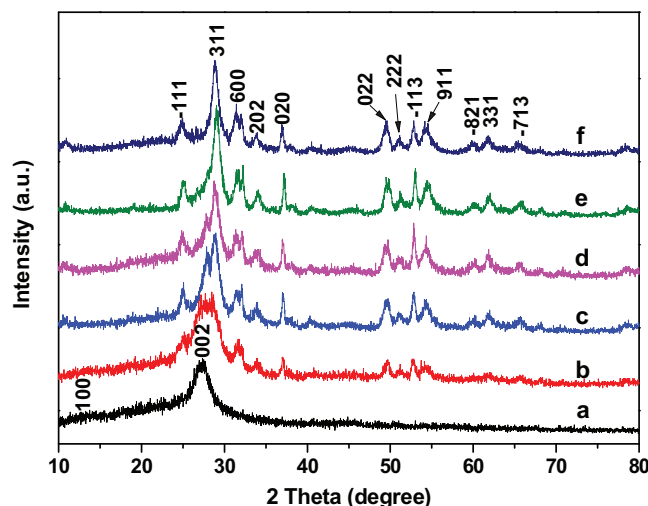

Fig. 4. XRD patterns of the as-prepared samples: (a) CN, (b) 10% SNO/CN, (c) 20% SNO/CN, (d) 30% SNO/CN, (e) 40% SNO/CN, and (f) SNO.

sample shows the typical 2D nanosheet structure with a lateral size of hundreds of nanometers and very thin thickness. After incorporating with CN nanosheets, it is clear that the SNO nanosheets maintain their 2D sheetlike structure during the synthetic process and integrate compactly on CN nanosheets surface to form well-defined 2D/2D heterostructures with an intimate interface (Fig. 1d). The interfacial interaction arised from such intimate 2D interface will be identified by the following FT-IR and XPS analyses. The HRTEM image of the 30% SNO/CN heterojunction in Fig. 1e displays distinct lattice fringes with a lattice spacing of 0.30 and 0.36 nm, corresponding to the lattice spacings of (3 1 1) and (−1 1 1) of monoclinic SNO, again confirming the formation of the SNO/CN heterostructures. Similarly, the well-defined 2D interface can be also found in the other SNO/CN heterostructure samples with different SNO contents (Fig. 2).

To further investigate the microstructure and composition of SNO/CN heterostructure, high-angle annular dark-field scanning transmission electron microscopy (HAADF-STEM) and EDX elemental scanning analysis were performed. As shown in Fig. 3, combined with the STEM image, the EDX mapping of elements C and N in the same region verifies the composition of CN. Similarly, Sn-L, Nb-L and O-K have the same shape and location, demonstrating the definite existence of SNO nanosheet in the heterostructure. This result gives solid evidence that SNO nanosheets are successfully incorporating with CN, forming the 2D/2D heterostructures.

Fig. 4 displays the XRD patterns of pristine CN, SNO, and SNO/CN heterostructures. For the CN sample, the XRD pattern reveals two distinct diffraction peaks at 13.0° and 27.4° (Fig. 4a), which can be indexed to the (002) and (100) diffraction planes of CN, respectively [48]. As shown in Fig. 4f, the main diffraction peaks of SNO at 24.7°, 29.0°, 31.3°, 34.1°, 36.8°, 49.7°, 51.0°, 53.0°, 54.5°, 59.7°, 61.6°, and 65.6°, correspond to the diffractions of (−1 1 1), (3 1 1), (6 0 0), (2 0 2), (0 2 0), (0 2 2), (2 2 2), (−1 1 3), (9 1 1), (−8 2 1), (3 3 1), and (−7 1 3) planes of monoclinic SNO (JCPDS, no. 84-1810) [49], respectively. No impurity peaks for SnO$_2$ or Nb$_2$O$_5$ were detected, indicating that pure SNO can be successfully prepared by the current hydrothermal method. Notably, the two characteristic peaks for CN gradually decreased in intensity with increasing amount of SNO, whereas the diffraction peaks of SNO intensified gradually (Fig. 4b–e), reflecting the existence of both SNO and CN in the heterostructures.

The composition and structure of the SNO/CN heterostructures were further confirmed by FT-IR spectra. As shown in Fig. 5, the peaks located at 1640, 1258, 1323, 1407, and 1568 cm^{-1} are
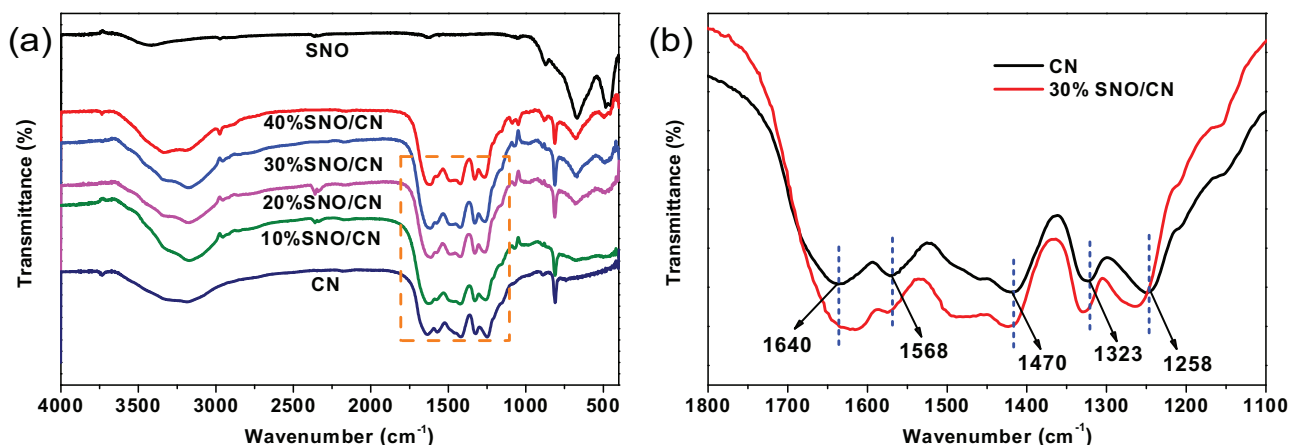
Fig. 5. (a) FT-IR spectra of SNO/CN heterostructures with different contents of SNO, (b) the magnified curves in the range of 1800 cm^{-1} to 1100 cm^{-1}.

attributable to the typical stretching vibration modes of the CN heterocycles. The peak near 808 cm^{-1} is assignable to the characteristic breathing mode of triazine units [13]. The absorption peaks of SNO appearing at 450, 480 and 670 cm^{-1} are ascribed to the characteristic internal Nb—O vibrational modes in the NbO$_6$ octahedron [50]. The main characteristic peaks ascribed to CN and SNO appear in SNO/CN heterostructures. However, of particular note is that, take the 30% SNO/CN heterostructure as example, the characteristic peak at 1640 cm^{-1} is shifted to lower wavenumbers, while the characteristic peaks centred at 1258, 1323, 1407, and 1568 cm^{-1} are shifted to higher wavenumbers. It is deduced that these shifts might be ascribed to a partial electron transfer from electron-rich structure of CN to SNO in the SNO/CN heterostructure, which will enhance the dispersibility of electron of SNO and CN and subsequently resulted in the reduction of vibration intensity of C=N and enhancement of vibration intensity of C—N, respectively. This result indicates that there might be some interfacial interactions in the SNO/CN heterostructures. This conclusion can be further confirmed by the XPS analysis.

XPS analysis was carried out to analyze the surface chemical composition and chemical states of CN, SNO and 30% SNO/CN samples. As shown in Fig. 6a, the XPS survey spectrum had peaks corresponding to Sn, Nb, O, N and C, consistent with the formation of a SNO/CN heterojunction. Two peaks at 485.7 and 494.1 eV correspond to the binding energy of Sn 3d$_{5/2}$ and Sn 3d$_{3/2}$ of SNO (Fig. 6b), indicating that Sn was present in the Sn^{2+} chemical state [51]. However, when combined with CN, the Sn 3d peak of 30% SNO/CN displays a slight shift towards the low binding energy compared to bare SNO. The spin orbit separation of Nb 3d is 2.8 eV and the Nb 3d$_{5/2}$ core level peak appears at 206.2 eV (Fig. 6c), demonstrating that the oxidation state of Nb element in the SNO is Nb^{5+} [52]. Correspondingly, this Nb 3d peak in the 30% SNO/CN sample also displays a slight shift compared to SNO. These shifts (Fig. 6b and c) in XPS measurement could be attributed to the presence of strong interactions at the interfaces between CN and SNO. Additionally, the O 1s XPS spectra of 30% SNO/CN can be deconvoluted into three peaks located at 529.8, 531.2 and 533.0 eV, respectively (Fig. 6d). The former binding energy peak corresponds to the O 1s core level of the O^{2-} anions in the SNO crystal lattice, while the latter bind-

ing energy peaks are probably attributed to surface contamination, such as hydroxides [53,54].

The N 1s XPS spectrum for the CN and 30% SNO/CN samples are shown in Fig. 6e. For the CN sample, the main peak of N 1s centred at 397.7 eV is derived from sp^2-hybridized N atoms (C=N—C) [55], while this peak is shift to 398.0 eV for the 30% SNO/CN heterostructure. On the other hand, as shown in Fig. 6f, the two peaks for C 1s centered at 284.6 eV and 287.2 eV are assigned to the surface adventitious reference carbon [56] and sp^2-hybridized carbon in the aromatic ring, respectively [57]. As expected, the C 1s peak at 287.5 eV of the 30% SNO/CN is also slightly shifted towards high binding energy compared to the pure CN. On the basis of the above XPS as well as FT-IR results, it can be concluded that there is strong interfacial interaction between the CN and SNO, which could facilitate the transfer of photoinduced charge and consequently improve the photocatalytic activity of SNO/CN heterostructures.

In order to characterize the specific surface area and pore characteristic of the as-prepared 30% SNO/CN heterostructure as well as pristine CN and SNO, we carried out the N$_2$ sorption analysis. As depicted in Fig. 7, typical IV isotherms with a typical H3 hysteresis loop were clearly seen on three samples, indicating the formation of micropores and mesopores [58]. The BET surface areas of the pristine CN, SNO, and 30% SNO/CN are determined to be ca. 42.98, 35.15 and 41.03 m^2 g^{-1}, respectively. The pore-size distribution of the samples are estimated using the Barrett–Joyner–Halenda (BJH) method from the desorption branch of the isotherm, as shown in the inset of Fig. 7. For clear comparison, the specific surface area, pore volume and pore size distribution of CN, SNO, and 30% SNO/CN are summarized in Table 1. Considering the BET results, it can be concluded that the surface area of these photocatalysts is not the critical factor to determine catalytic efficiency of the photocatalysts.

3.2. Optical properties

The light absorption properties of pristine CN, SNO, and SNO/CN heterostructures were characterized by UV–vis diffuse reflectance spectroscopy. Fig. 8a shows the optical absorption edges of pristine CN and SNO were roughly estimated from the absorption

Table 1
Measured parameters for CN, SNO, and 30% SNO/CN heterostructure.

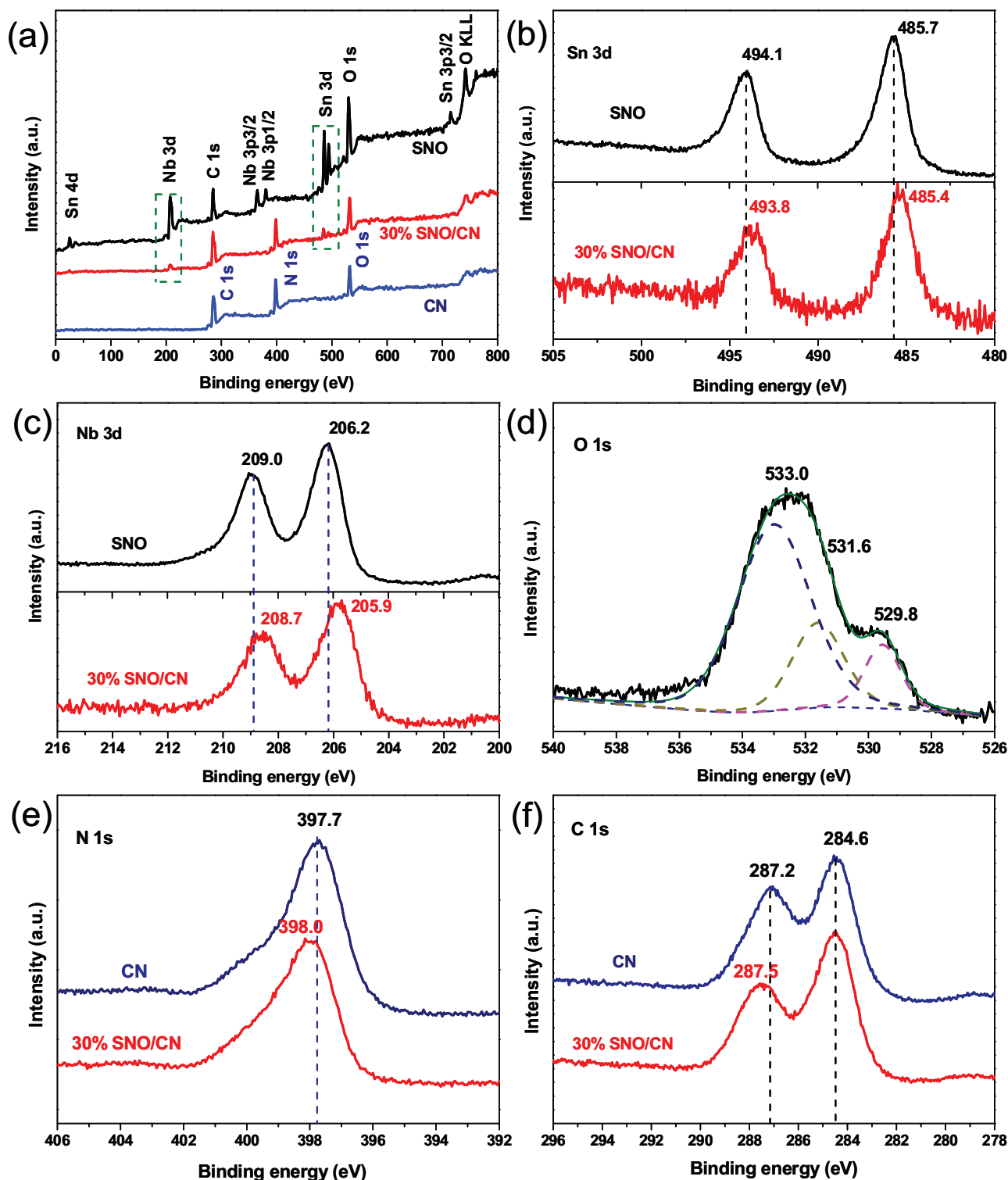| Samples	Surface area (m^2 g^{-1})	Pore volume (cm^3 g^{-1})	Average pore size (nm)	Kinetic rate constant (K) (h^{-1})
CN	35.15	0.022	12.66	0.26494
SNO	42.98	0.021	11.74	0.32741
30% SNO/CN	41.03	0.083	13.80	1.03847

Fig. 6. XPS spectra of the pure SNO, CN, and 30% SNO/CN heterostructure. (a) survey spectrum, (b) Sn 3d, (c) Nb 3d, (d) O 1s, (e) N 1s, and (f) C 1s.

onset and they located approximately at about 530 and 440 nm, respectively. The visible light absorption intensity is enhanced with increasing SNO content in the SNO/CN heterostructures. This can be observed from the color change of the samples, which changes from cream–yellow to orange with increasing SNO content (Inset in Fig. 8a). It is inferred that this enhanced light absorption is beneficial to generate more electron–hole pairs and then lead to an enhanced photocatalytic activity.

The energy level and band gap of the semiconductors plays a crucial role in determining its physical properties. The band gap energy (E_g) of a semiconductor can be calculated by the following formula:

$$\alpha h\upsilon = A(h\upsilon - E_g)^{n/2} \tag{1}$$

where α, h, υ, E_g and A are optical absorption coefficient, Planck constant, light frequency, band gap energy, and a constant, respec-
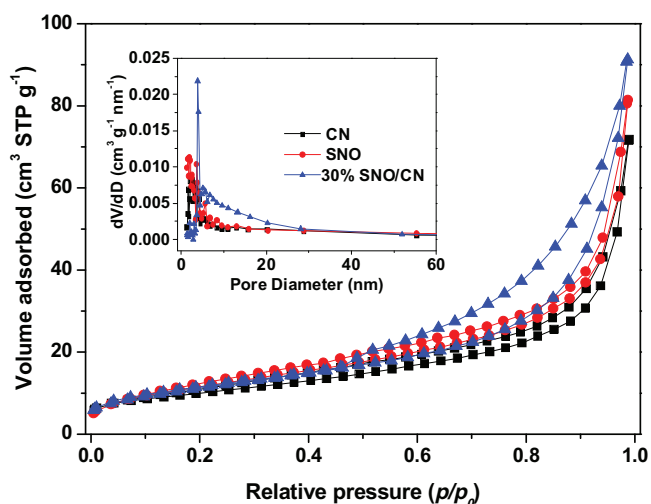
Fig. 7. Nitrogen sorption isotherm and Barrett–Joyner–Halenda (BJH) pore size distribution plot (inset) of CN, SNO, and 30% SNO/CN heterostructure.
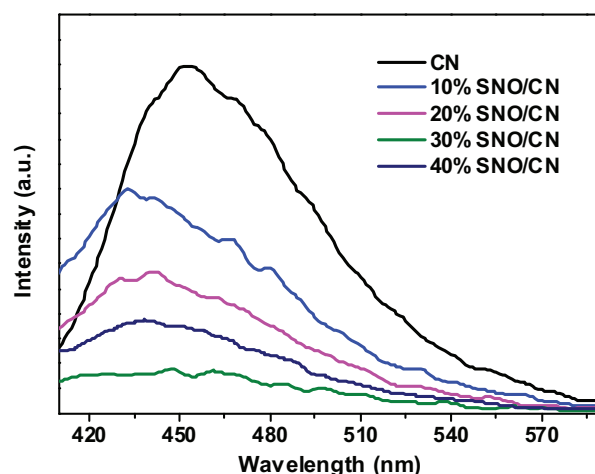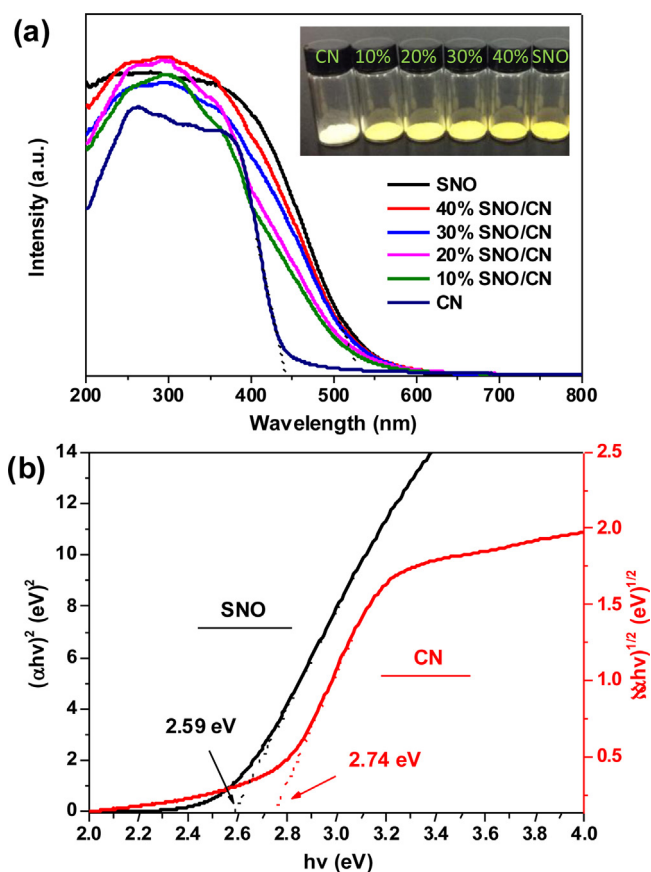

Fig. 8. (a) UV–vis diffuse reflectance spectra of pristine CN, SNO nanosheet, and SNO/CN heterostructures. Inset shows the photos of the samples. (b) Plot of $(\alpha h\upsilon)^{1/2}$ vs. $h\upsilon$ for the band gap energy of CN and plot of $(\alpha h\upsilon)^2$ vs. $h\upsilon$ for the band gap energy of SNO.

tively [59]. Among them, n is determined from the type of optical transition of a semiconductor ($n = 1$ for direct transition and $n = 4$ for indirect transition). The E_g of CN was found to be 2.74 eV according to a plot of $(\alpha h\upsilon)^{1/2}$ versus energy ($h\upsilon$) (Fig. 8b). Accordingly, the E_g of SNO was determined from a plot of $(\alpha h\upsilon)^2$ versus energy ($h\upsilon$) (Fig. 8b) and the band gap energy of SNO is approximately 2.59 eV.

Fig. 9. Room temperature PL spectra of CN and SNO/CN heterostructures under the excitation wavelength of 325 nm.

Both the band gap values of CN and SNO are very close to previously reported results [48,60].

3.3. Charge transfer properties

Photoluminescence (PL) spectra has been performed to reveal the charge transfer, migration and recombination processes of the SNO/CN heterostructures since PL emission arises from the recombination of free carriers. Fig. 9 presents the PL spectra of the SNO/CN photocatalysts at an excitation wavelength of 325 nm. At room temperature, the emission band for pure CN was centered at 460 nm, which was attributed to the radiative recombination process of self-trapped excitations [17]. However, the PL intensity of the SNO/CN heterostructures decreased significantly compared to bare CN. The fluorescence quenching via coupling SNO nanosheets mainly results from improved interfacial charge transfer between SNO and CN nanosheets, which could improve the separation of electron–hole pairs in the excited heterojunction, leading to the enhanced photocatalytic activity.

To further understand the photogenerated charge separation and electron transfer performance between CN and SNO, the transient photocurrent responses of pristine CN, SNO and 30% SNO/CN heterostructure electrodes were recorded for several on-off cycles under visible light irradiation, as shown in Fig. 10a. As expected, the 30% SNO/CN heterostructure exhibits the highest photocurrent response than that of pristine CN and SNO, which indicates that a greatly improved charge separation exists at the 2D interface in the 30% SNO/CN. Electrochemical impedance spectroscopy (EIS) of pristine CN, SNO, and 30% SNO/CN heterostructure was also carried out to provide additional evidence for the improved charge separation in the SNO/CN heterojunction, and the result is shown in Fig. 10b. The radius of the arc on the EIS Nyquist plot reflects the charge transfer rate occurring at the contact interface between the working electrode and electrolyte solution. Generally, the smaller radius of the Nyquist circle represents the lower charge-transfer resistance. As displayed in Fig. 10b, the arc radius on EIS Nyquist plot of 30% SNO/CN heterostructure is smaller than that of pristine CN and SNO. The lowest impendance value for the 30% SNO/CN heterojunction again indicates the fastest separation and transfer rate of electrons and holes in the 2D/2D heterostructures, which is beneficial to the enhanced photocatalytic activity. This point will be confirmed by the photocatalytic activity results.
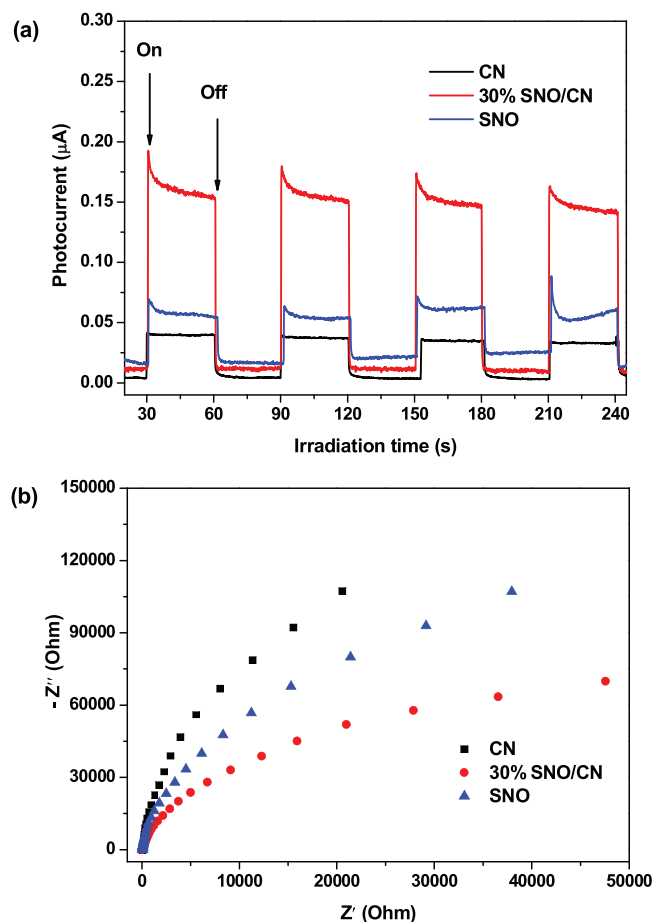
Fig. 10. (a) Transient photocurrent response and (b) Nyquist plots of EIS obtained for pristine CN, SNO, and 30% SNO/CN heterostructure.

Fig. 11. (a) Photocatalytic degradation of MB in the presence of pristine CN, SNO, and SNO/CN heterostructures and photolysis of MB under visible light irradiation and (b) kinetic fit for the degradation of MB with pristine CN, SNO, and SNO/CN heterostructures.

3.4. Photocatalytic activity and stability

The photocatalytic activities of the as-prepared SNO/CN 2D/2D heterostructures were examined by the degradation of MB in aqueous solution under visible light irradiation, and the results are shown in Fig. 11a. Prior to illumination, the suspension was magnetically stirred for 60 min in the dark to achieve the adsorption equilibrium of the MB on the photocatalyst powders. Control experiments in the absence of visible light irradiation indicated that the pure SNO nanosheet sample has much higher capacity towards the adsorption of MB (about 55% after 60 min) as compared to other samples. The relatively large surface area and negatively charged surface of SNO sample could partially account for the facile MB adsorption [47]. In the absence of photocatalyst, the direct photolysis of MB is inappreciable within the test period, suggesting that photolysis of MB is negligible. As shown in Fig. 11a, the degradation ratios of MB in the presence of pristine SNO and CN only reach 70% and 62% in 4 h, respectively. As expected, all of the SNO/CN heterostructures exhibited higher photocatalytic activity than the bare SNO and CN under the same experimental conditions. The photocatalytic activity trend follows the order 30% SNO/CN > 40% SNO/CN > 20% SNO/CN > 10% SNO/CN. When the optimum content of the SNO was located at 30%, the highest photocatalytic activity of SNO/CN was obtained. The 30% SNO/CN heterostructure could degrade approximately 99% of MB in 4 h with a reaction rate constant of $1.04\,h^{-1}$, which is about 3.9 times that of pristine CN (Fig. 11b and Table 1). Excess SNO content in the heterostructures leads to a decrease of photocatalytic activity, which could be understood through considering the integrated effects
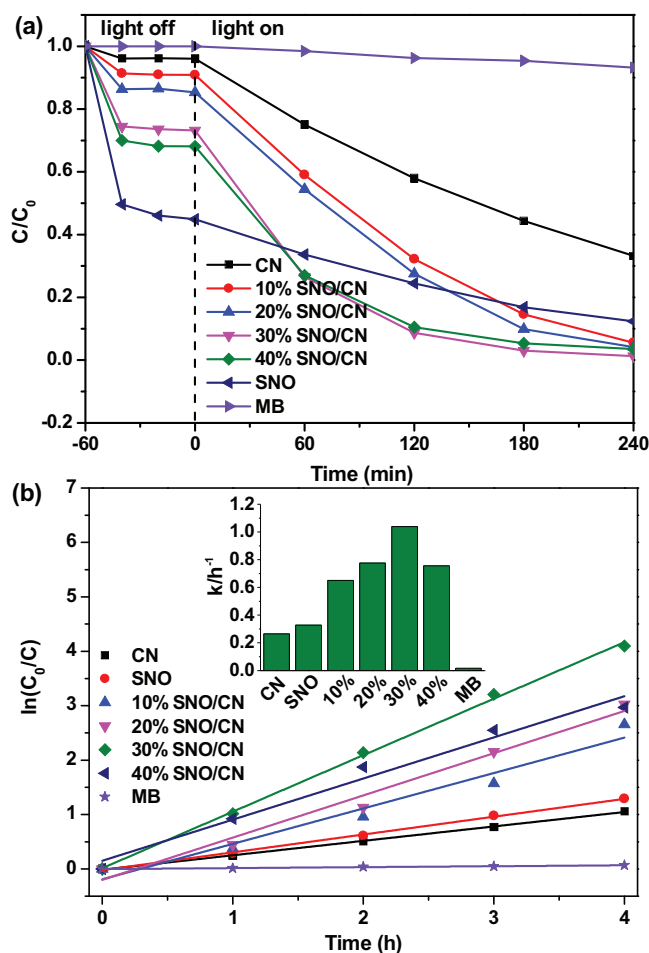
of light absorption and heterojunction structure of SNO/CN. As the SNO content increased, the visible light absorption of SNO/CN strengthened and generated more electron–hole pairs, and more SNO/CN heterojunction was formed, contributing to the separation of electron–hole pairs. When the SNO content was above the optimal value, the efficient heterojunction interface did not increase significantly. The excessive narrow band-gap SNO might act as the recombination center of electrons and holes to consequently restrain the photocatalytic activity.

The reusability and stability of the photocatalyst are vital to the practical application. Taking 30% SNO/CN heterostructure as the representative photocatalyst, the regeneration and reusability of SNO/CN is investigated. For each recycling run, SNO/CN is collected by centrifugation, and then washed with ethanol for three times. As shown in Fig. 12a, no apparent deactivation of the photocatalyst was observed after four consecutive runs, which implies the high stability of the 30% SNO/CN heterostructure. Fig. 12b compares the XRD patterns of the 30% SNO/CN heterostructure before and after the photocatalytic reaction. It can be found that the XRD pattern of recycled 30% SNO/CN heterostructure has almost no change compared with the unirradiated one, indicating that the as-prepared catalyst is sufficiently stable during the photodegradation of organic dye.
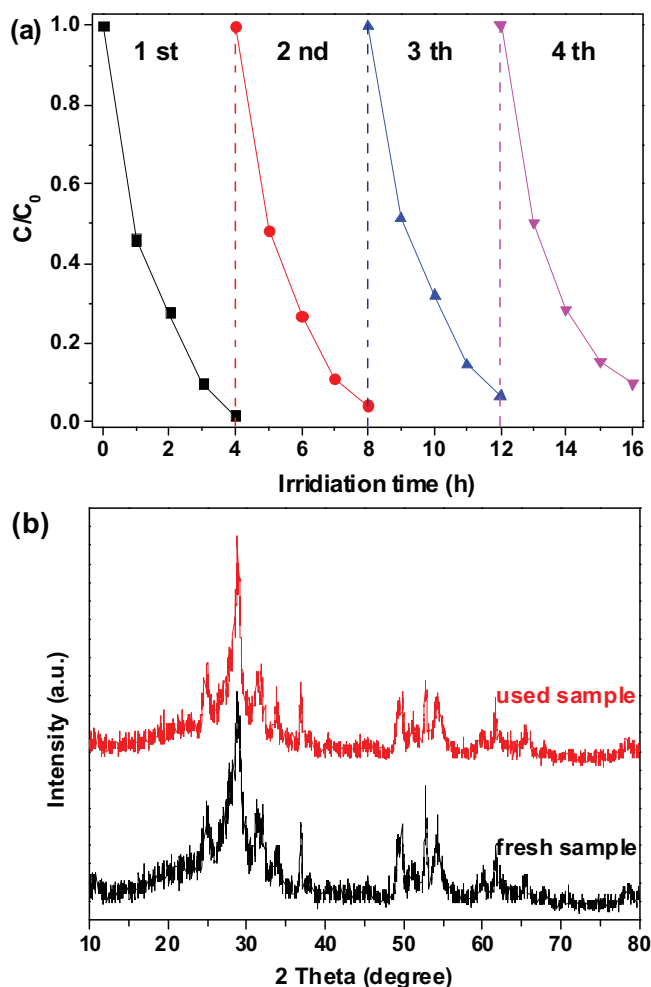
Fig. 12. (a) Cycling runs for the photodegradation of MB in the presence of 30% SNO/CN heterostructure under visible light irradiation; (b) XRD patterns of the 30% SNO/CN heterostructure before and after the 4-cycle reaction.

3.5. Possible photocatalytic mechanism

In order to ascertain the active species in the degradation process, some sacrificial agents, such as *tert*-butanol (*t*-BuOH), ammonium oxalate (AO) and 1,4-benzoquinone (BQ) were employed as the hydroxyl radical ($\bullet$OH) scavenger, hole (h^+) scavenger and superoxide radical ($\bullet O_2^-$) scavenger, respectively. As shown in Fig. 13, when 1 mmol of *t*-BuOH as scavenger for $\bullet$OH radical species was added, the degradation of MB was slightly depressed, indicating that few $\bullet$OH was involved in the degradation of MB. Whereas the rate for degradation of MB over 30% SNO/CN sample was depressed obviously with 1 mmol of AO as a hole scavenger added to the solution, indicating that the active species of holes play an important role toward the degradation of MB. Notably, with the addition of 1 mmol of $\bullet O_2^-$ scavenger BQ, the degradation of MB was also significantly depressed, suggesting that the $\bullet O_2^-$ pathway has a crucial role in the process of MB oxidation. To further confirm this point, a N_2 purging experiment was conducted compared with air-equilibrated conditions. The removal efficiency of MB is obviously inhibited by conducted N_2 (no scavenger, N_2) compared with air-equilibrated conditions (blank), which shows that dissolved oxygen which can act as a photogenerated electron scavenger to give $\bullet O_2^-$ radical species, which are pivotal for the MB degradation. Based on these results, it can be preliminarily concluded that h^+ and $\bullet O_2^-$ are the major reactive species of SNO/CN heterostructures for degradation of MB.
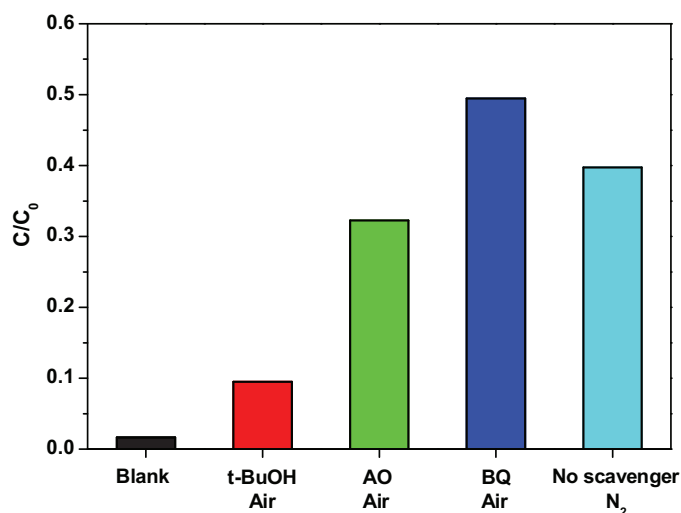

Fig. 13. Trapping experiment of active species during the photocatalytic degradation of MB over 30% SNO/CN heterostructure under visible light irradiation.
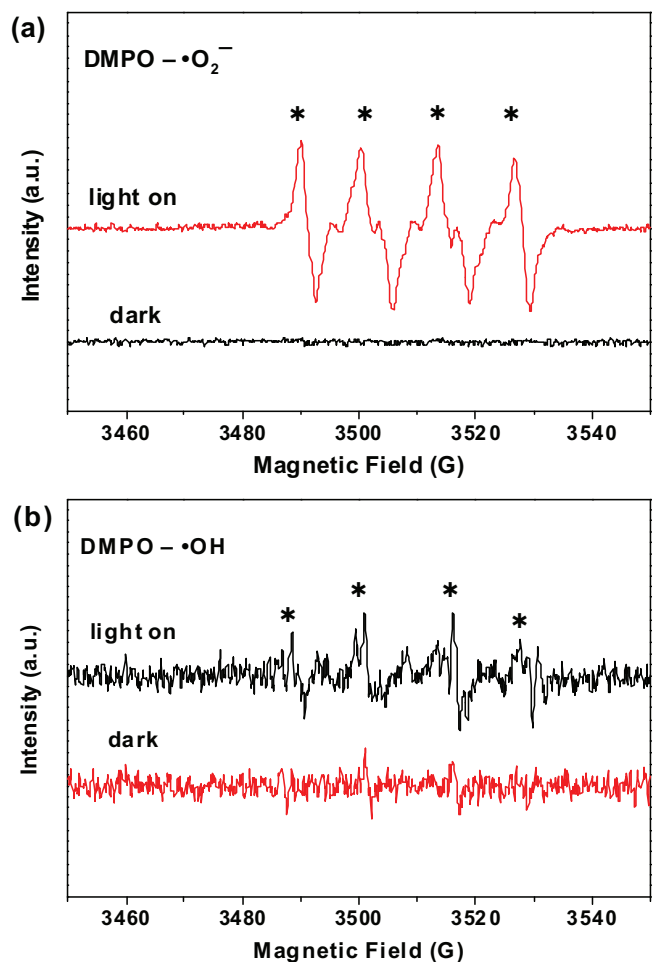

Fig. 14. DMPO spin-trapping ESR spectra for 30% SNO/CN: (a) in methanol dispersion for DMPO–$\bullet O_2^-$ and (b) in aqueous dispersion for DMPO–$\bullet$OH.

To further identify the radical generation in this photocatalytic system under visible light irradiation, the ESR spin-trap with DMPO technique was carried out on illuminated 30% SNO/CN heterojunction. Fig. 14a presents ESR spectra measured as the effect of light irradiation on the 30% SNO/CN heterojunction at room tempera-
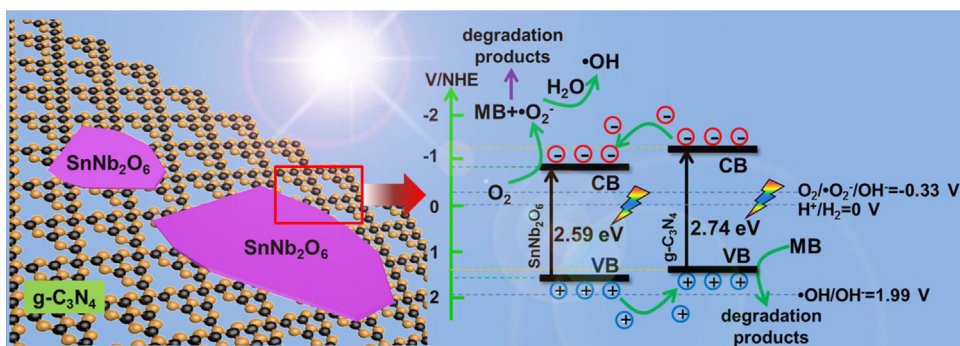
Fig. 15. Proposed mechanisms of charge transfer and dye degradation in the SNO/CN heterostructure under visible light irradiation.

ture in air. There is no ESR signal in the dark. When the light is on, the characteristic signals of the DMPO–•O_2^- could be observed, further confirming the formation of •O_2^- during the photocatalytic process (Fig. 14a). In addition, the characteristic quadruple peaks of the DMPO–•OH adducts were also detected, but the peak intensity was extremely low (Fig. 14b), compared with the intensity of DMPO–•O_2^- adducts. Therefore, it can be concluded that the •O_2^- radicals plays an important role in the photodegradation process and few •OH radicals just participate in the photocatalytic reaction.

On the basis of the above experimental results, a synergistic mechanism for degradation of MB over the SNO/CN 2D/2D heterostructures was proposed, as illustrated in Fig. 15. Since the conduction band (CB) edge potential of CN (−1.21 V vs. NHE) was more negative than the CB edge of SNO (−0.99 V vs. NHE), the photogenerated electrons in the CB edge of CN injected directly to the CB of SNO under visible light irradiation, while the holes generated in the VB of SNO could migrate to the surface of CN. Consequently, the photogenerated electrons and holes were spatially separated at the SNO/CN 2D nanosheets interfaces. The accumulated electrons in the CB of SNO can be transferred to O_2 adsorbed on the surface of the heterostructures and •O_2^- yields because the CB edge potential of SNO is more negative than the standard redox potential $E^0(O_2/•O_2^-)$ (−0.33 V vs. NHE) [61,62]. At the same time, rich holes in the VB of CN have powerful potential to oxidize MB directly. However, the holes cannot oxidize OH$^-$ or H_2O to •OH radicals, because the VB position of CN (1.53 V vs. NHE) is more negative than the standard redox potential of $E^0(•OH/OH^-)$ (1.99 V vs. NHE) [61]. So, the few •OH radicals are possibly originated from the reaction of •O_2^- with photogenerated electrons. As a result, the separated electrons and holes can be fully involved in photocatalytic reactions, and a highly corresponding activity is achieved.

4. Conclusions

To summarize, we have successfully constructed a novel 2D/2D heterostructure comprising of SNO and CN nanosheets by using a simple two-step wet chemistry method. The SNO/CN heterostructures exhibited remarkably enhanced photocatalytic performance toward degradation of MB as compared to pristine CN and SNO. The optimum photocatalytic activity of 30% SNO/CN for the degradation of MB was about 3.9 and 3.2 times higher than those of pristine CN and SNO. The enhanced photocatalytic activity could be attributed to the synergistic effect of 2D/2D heterostructures with strong interfacial interaction and unique, abundant 2D coupling interfaces, which could lead to the improved photoinduced charges separation and further enhancement of photocatalytic activity. The photogenerated holes and superoxide radicals are the two main photoactive species toward photocatalytic degradation of MB over SNO/CN heterostructures. The present research is expected to be helpful for the

design and construction of novel 2D/2D heterostructures with high or enhanced photocatalytic activity.

References

[1] H. Tong, S.X. Ouyang, Y.P. Bi, N. Umezawa, M. Oshikiri, J.H. Ye, Adv. Mater. 24 (2012) 229–251.
[2] X.B. Chen, S.H. Shen, L.J. Guo, S.S. Mao, Chem. Rev. 110 (2010) 6503–6570.
[3] H.L. Zhou, Y.Q. Qu, T. Zeid, X.F. Duan, Energy Environ. Sci. 5 (2012) 6732–6743.
[4] D.Q. Zhang, M.C. Wen, S.S. Zhang, P.J. Liu, W. Zhu, G.S. Li, H.X. Li, Appl. Catal. B: Environ. 147 (2014) 610–616.
[5] K. Zhang, L.J. Guo, Catal. Sci. Technol. 3 (2013) 1672–1690.
[6] C.S. Pan, T. Takata, M. Nakabayashi, T. Matsumoto, N. Shibata, Y. Ikuhara, K. Domen, Angew. Chem. Int. Ed. 54 (2015) 2955–2959.
[7] L.Z. Wu, B. Chen, Z.J. Li, C.H. Tung, Acc. Chem. Res. 47 (2014) 2177–2185.
[8] X.C. Wang, K. Maeda, A. Thomas, G. Takanabe, G. Xin, J.M. Carlsson, K. Domen, M. Antonietti, Nat. Mater. 8 (2009) 76–80.
[9] J. Liu, Y. Liu, N.Y. Liu, Y.Z. Han, X. Zhang, H. Huang, Y. Lifshitz, S.T. Lee, J. Zhong, Z.H. Kang, Science 347 (2015) 970–974.
[10] D.J. Martin, K.P. Qiu, S.A. Shevlin, A.D. Handoko, X.W. Chen, Z.X. Guo, J.W. Tang, Angew. Chem. Int. Ed. 53 (2014) 9240–9245.
[11] S.C. Yan, Z.S. Li, Z.G. Zou, Langmuir 25 (2009) 10397–10401.
[12] J. Mao, T.Y. Peng, X.H. Zhang, K. Li, L.Q. Ye, L. Zan, Catal. Sci. Technol. 3 (2013) 1253–1260.
[13] D.L. Jiang, L.L. Chen, J.J. Zhu, M. Chen, W.D. Shi, J.M. Xie, 2013, Dalton Trans. 42 (2013) 15726–15734.
[14] J.S. Zhang, X.F. Chen, K. Takanabe, K. Maeda, K. Domen, J.D. Epping, X.Z. Fu, M. Antonietti, X.C. Wang, Angew. Chem. Int. Ed. 49 (2010) 441–444.
[15] S.W. Cao, J.G. Yu, J. Phys. Chem. Lett. 5 (2014) 2101–2107.
[16] D.L. Jiang, J.J. Zhu, M. Chen, J.M. Xie, J. Colloid Interface Sci. 417 (2014) 115–120.
[17] L. Ge, C.C. Han, J. Liu, Appl. Catal. B: Environ. 100 (2011) 108–109.
[18] X.X. Xu, G. Liu, C. Randorn, J.T.S. Irvine, Int. J. Hydrog. Energy 36 (2011) 13501–13507.
[19] G.G. Zhang, S.H. Zang, X.C. Wang, ACS Catal. 5 (2015) 941–947.
[20] Y.J. Cui, Z.X. Ding, X.Z. Fu, X.C. Wang, Angew. Chem. Int. Ed. 51 (2012) 11814–11818.
[21] M. Zhang, J. Xu, R.L. Zong, Y.F. Zhu, Appl. Catal. B: Environ. 147 (2014) 229–235.
[22] G. Liu, P. Niu, C.H. Sun, S.C. Smith, Z.G. Chen, G.Q. Lu, H.M. Cheng, J. Am. Chem. Soc. 132 (2010) 11642–11648.
[23] Z.Z. Lin, X.C. Wang, Angew. Chem. Int. Ed. 52 (2013) 1735–1738.
[24] J.S. Zhang, G.G. Zhang, X.F. Chen, S. Lin, L. Mçhlmann, G. Dołega, G. Lipner, M. Antonietti, S. Blechert, X.C. Wang, Angew. Chem. Int. Ed. 124 (2012) 3237–3241.
[25] S. Chu, Y. Wang, Y. Guo, J.Y. Feng, C.C. Wang, W.J. Luo, X.X. Fan, Z.G. Zou, ACS Catal. 3 (2013) 912–919.
[26] A.K. Singh, K. Mathew, H.L. Zhuang, R.G. Hennig, J. Phys. Chem. Lett. 6 (2015) 1087–1098.
[27] J.L. Gunjakar, I.Y. Kim, J.M. Lee, Y.K. Jo, S.J. Hwang, J. Phys. Chem. C 118 (2014) 3847–3863.
[28] Y.F. Sun, Y. Gao, Y. Xie, Chem. Soc. Rev. 43 (2014) 530–546.
[29] I.Y. Kim, J.M. Lee, T.W. Kim, H.N. Kim, H. Kim, W.Y. Choi, S.J. Hwang, Small 8 (2012) 1038–1048.

[30] J. Sun, H. Zhang, L.H. Guo, L.X. Zhao, ACS Appl. Mater. Interfaces 5 (2013) 13035–13041.
[31] P. Chen, Y. Su, H. Liu, Y. Wang, ACS Appl. Mater. Interfaces 5 (2013) 12073–12082.
[32] W.J. Zhou, Z.Y. Yin, Y.P. Du, X. Huang, Z.Y. Zeng, Z.X. Fan, H. Liu, J.Y. Wang, H. Zhang, Small 9 (2013) 140–147.
[33] W.G. Tu, Y. Zhou, Q. Liu, Z.P. Tian, J. Gao, X.Y. Chen, H.T. Zhang, J.G. Liu, Z.G. Zou, Adv. Funct. Mater. 22 (2012) 1215–1221.
[34] J. Sun, H. Zhang, L.H. Guo, L.X. Zhao, ACS Appl. Mater. Interfaces 5 (2013) 13035–13041.
[35] Z.Y. Zhan, J.D. Huang, M.Y. Zhang, Q. Yuan, B. Dong, Appl. Catal. B: Environ. 163 (2015) 298–305.
[36] Y.D. Hou, A.B. Laursen, J.S. Zhang, G.G. Zhang, Y.S. Zhu, X.C. Wang, S. Dahl, I. Chorkendorff, Angew. Chem. Int. Ed. 52 (2013) 3621–3625.
[37] S.W. Hu, L.W. Yang, Y. Tian, X.L. Wei, J.W. Ding, J.X. Zhong, P.K. Chu, Appl. Catal. B: Environ. 163 (2015) 611–622.
[38] Y. Hou, Z.H. Wen, S.M. Cui, X.R. Guo, J.H. Chen, Adv. Mater. 25 (2013) 6291–6297.
[39] Y. Okamoto, S. Ida, J. Hyodo, H. Hagiwara, T. Ishihara, J. Am. Chem. Soc. 133 (2011) 18034–18037.
[40] K. Maeda, M. Eguchi, T. Oshima, Angew. Chem. Int. Ed. 53 (2014) 13164–13168.
[41] T.G. Xu, C. Zhang, X. Shao, K. Wu, Y.F. Zhu, Adv. Funct. Mater. 16 (2006) 1599–1607.
[42] S.J. Liang, R.W. Liang, L.R. Wen, R.S. Yuan, L. Wu, X.Z. Fu, Appl. Catal. B 125 (2012) 103–110.
[43] K. Saito, A. Kudo, Inorg. Chem. 52 (2013) 5621–5623.
[44] L.P. Cruz, J.-M. Savariault, J. Rocha, J.-C. Jumas, J.D. Pedrosa de Jesus, J. Solid State Chem. 156 (2001) 349–359.
[45] D. Chen, J. Ye, Chem. Mater. 21 (2009) 2327–2333.
[46] Y. Hosogi, K. Tanabe, H. Kato, H. Kobayashi, A. Kudo, Chem. Lett. 33 (2004) 28–29.
[47] L. Yuan, M.Q. Yang, Y.J. Xu, Nanoscale 6 (2014) 6335–6345.
[48] S.C. Yan, Z.S. Li, Z.G. Zou, Langmuir 26 (2010) 3894–3901.
[49] I.C.M.S. Santos, L.H. Loureiro, M.F.P. Silva, M.V. Cavaleiro, Polyhedron 21 (2002) 2009–2015.
[50] A.E. Lavat, E.J. Baran, Vibr. Spectrosc. 32 (2003) 167–174.
[51] Q.Y. Li, T. Kako, J.H. Ye, Int. J. Hydrog. Energy 36 (2011) 4716–4723.
[52] V.V. Atuchin, I.E. Kalabin, V.G. Kesler, N.V. Pervukhina, J. Electron Spectrosc. Relat. Phenom. 142 (2005) 129–134.
[53] C.R. Clayton, Y.C. Lu, J. Electrochem. Soc. 133 (1986) 2465–2473.
[54] J. Ding, L. Wang, Q. Liu, Y. Chai, X. Liu, W.L. Dai, Appl. Catal. B: Environ. 176 (2015) 91–98.
[55] B. Chai, T.Y. Peng, J. Mao, K. Li, L. Zan, Phys. Chem. Chem. Phys. 14 (2012) 16745–16752.
[56] X. Yang, Y.H. Wang, L.L. Xu, X.D. Yu, Y.H. Guo, J. Phys. Chem. C 112 (2008) 11481–11489.
[57] F.F. Shi, L.L. Chen, C.S. Xing, D.L. Jiang, D. Li, M. Chen, RSC Adv. 4 (2014) 62223–62229.
[58] K.S.W. Sing, D.H. Everett, R.A.W. Haul, L. Moscou, R.A. Pierotti, J. Rouquerol, Pure Appl. Chem. 57 (1985) 603–619.
[59] M.A. Butler, J. Appl. Phys. 48 (1977) 1914.
[60] S.J. Liang, S.Y. Zhu, Y. Chen, W.M. Wu, X.C. Wang, L. Wu, J. Mater. Chem. 22 (2012) 2670–2678.
[61] X.L. Fu, W.M. Tang, L. Ji, S.F. Chen, Chem. Eng. J. 180 (2012) 170–177.
[62] Z.H. Li, Z.P. Xie, Y.F. Zhang, L. Wu, X.X. Wang, X.Z. Fu, J. Phys. Chem. C 111 (2007) 18348–18352.